Hyperspectral and Nanosecond Temporal Resolution Widefield Infrared Photothermal Heterodyne Imaging

Kirill Kniazev[a], Evgenii Zaitsev[a], Shubin Zhang[b], Yang Ding[a], Loc Ngo[a], Zhuoming Zhang[a], Gregory V. Hartland[a], Masaru Kuno[a,b,*]

Affiliations:

[a]Department of Chemistry and Biochemistry, University of Notre Dame, Notre Dame, IN 46556

[b]Department of Physics and Astronomy, University of Notre Dame, Notre Dame, IN 46556

ORCID

Kirill Kniazev: 0000-0002-7338-1436
Yang Ding: 0000-0001-8437-3565
Loc Ngo: 0000-0001-9476-5335
Zhuoming Zhang: 0000-0002-0507-3546
Gregory Hartland: 0000-0002-8650-6891
Masaru Kuno: 0000-0003-4210-8514

*mkuno@nd.edu

Abstract:

Label-free, bond-selective imaging offers new opportunities for fundamental and applied studies in chemistry, biology, and materials science. Preventing its broader application to investigating spectrally congested specimens are issues related to low sensitivity as well as low spatial and temporal resolution. Here, we demonstrate a widefield, mid-infrared (MIR) photothermal imaging technique, called widefield Infrared Photothermal Heterodyne imaging (wIR-PHI), that massively parallelizes acquisition of MIR absorption data through use of a high-speed complementary metal-oxide-semiconductor camera. wIR-PHI possesses notable features that include: spatial resolution significantly below the MIR diffraction limit, hyperspectral imaging capabilities, high sensitivity, and ~100 ns temporal resolution. The first two features are highlighted by hyperspectral imaging of proximally close poly(methyl methacrylate) (PMMA) and polystyrene (PS) nanoparticles where clear, bond-specific imaging of nanoparticles, separated by less than the MIR diffraction limit, is demonstrated. Sensitivity is highlighted by imaging individual PMMA and PS nanoparticles with radii between r=97-556 nm. This leads to a current, peak absorption cross-section limit-of-detection of $\sigma_{abs}=1.9\times10^{-16}$ cm^2. wIR-PHI's 100 ns temporal resolution is simultaneously demonstrated by observing the decay of photothermal contrast on individual nanoparticles on a ~200-6000 ns timescale. In whole, wIR-PHI's dramatic increase in acquisition speed opens opportunities for future MIR kinetic imaging and spectroscopic studies of important chemical, biological, and material processes.

Keywords: Photothermal spectroscopy, Photothermal microscopy, Infrared imaging, Mid-infrared, Single particle.

Introduction

Vibrational optical spectroscopies stand as important, label-free imaging modalities for the complete structural and functional characterization of chemical, environmental and biological specimens.[1 6] Two major embodiments involve Raman scattering[13] and infrared (IR) absorption spectroscopy. Raman microscopy possesses a relatively high spatial resolution of ~300 nm. Unfortunately, small scattering cross-sections of ~10^{-30} cm^2 limit its overall applicability, especially within the context of ultrasensitive analytical detection.[14] Although IR spectroscopy exhibits significantly higher sensitivities due to absorption cross-sections nearly 12 orders of magnitude larger, a significant drawback is its lack of spatial resolution. Here, the Abbe diffraction limit[15] restricts IR-based techniques such as Fourier Transform Infrared (FTIR) spectroscopy[16] to a spatial resolution of 2.5-10 μm. This prevents IR techniques from being applied to high resolution microscopy and spectroscopy of specimens in spectrally congested environments.

Recently, a new super-resolution, infrared absorption spectroscopy that circumvents the Abbe diffraction limit has been developed. Called Infrared Photothermal Heterodyne Imaging (IR-PHI), the technique exhibits a ~300 nm spatial resolution.[11,17,18] This is achieved through photothermal heating[19] of specimens when a mid-infrared (MIR) pump laser is on resonance with a its characteristic, MIR vibrational transitions. Subsequent specimen refractive index and scattering cross-section changes are then detected using a second, visible wavelength (probe) laser. IR-PHI's spatial resolution is therefore dictated by the probe's diffraction limit, which, in turn, allows super-resolution MIR imaging and spectroscopy. More about IR-PHI and its implementation can be found in References 18, 21, and 22.

As demonstrated, IR-PHI involves raster scanning specimens below pump and probe foci. Application to dynamic, bond-selective imaging is therefore restricted. To address an open need, researchers have therefore pursued introducing a widefield modality to the technique.[23,24,25] Issues exist with these implementations, however, that restrict their use in dynamic imaging.[26]

Here, we introduce a ns-timescale, widefield modality to IR-PHI (called wIR-PHI) that utilizes nanosecond MIR pump pulses synchronized to the frame rate of a high-speed complementary metal-oxide-semiconductor (CMOS) camera. This enables large area MIR image acquisition as well as hyperspectral imaging capabilities when measurements are synchronized to the laser frequency. In what follows, wIR-PHI's capabilities are demonstrated through fast IR imaging of individual poly(methyl methacrylate) (PMMA) and polystyrene (PS) nanoparticles along with acquisition of bond-specific, hyperspectral data. By imaging individual PMMA and PS nanoparticles with radii (r) between r=97-556 nm, a peak experimental MIR absorption cross-section (σ_{abs}) limit-of-detection of $\sigma_{abs}=1.9\times10^{-16}$ cm^2 is established. Fast 100 ns temporal-resolution is demonstrated via measurements of single nanoparticle photothermal signal decay. Altogether, wIR-PHI enables super-resolution, hyperspectral imaging on fast timescales, opening up opportunities for future dynamic MIR measurements of important chemical, biological, and materials processes.

Instrumentation

Figure 1 outlines wIR-PHI's implementation. The employed MIR pump laser is a 20 kHz tunable IR optical parametric oscillator (Firefly, M-Squared) with a tuning range between 5.43-9.61 μm (1840-1040 cm^{-1}). MIR pump light is focused onto CaF_2-supported specimens with a high numerical aperture (NA) reflective Schwarzschild objective (Ealing, 0.65 NA). Pump intensities (I_{pump}) range from I_{pump}=18 to 360 MW cm^{-2}.

A visible, 532 nm, continuous wave (CW) laser serves as the probe wherein a high NA refractive objective (Nikon, 0.95 NA) focuses probe light onto the same region of the specimen. Pump and probe objectives are aligned in a counterpropagating pump/probe geometry[18,20] to maximize either IR-PHI's or wIR-PHI's spatial resolution. Widefield illumination is achieved by placing a 50 cm focal length plan convex lens prior to the refractive objective's back focal plane. Resulting probe illumination regions are thus of order 70 μm^2 with a corresponding wIR-PHI probe intensity of $I_{probe}\approx 40$ kW cm^{-2} (30 mW, 70 μm^2 illumination area). In the absence of a plan convex lens (as required for IR-PHI) the probe intensity is $I_{probe}\approx 230$ kW cm^{-2} (700 μW, 0.3 μm^2 illumination area). Scattered probe light from specimens is collected with the same refractive objective and for wIR-PHI is detected with a high-speed CMOS camera (Photron, Nova S12). For IR-PHI, a custom autobalanced photodiode is used.[27]

To generate wIR-PHI images, "hot" and "cold"[28] frames are acquired by synchronizing CMOS frame exposure with the MIR laser pulse train. Hot frames are acquired either synchronously or temporally offset from MIR pump pulses. Cold frames are acquired between MIR pulses. MIR laser and CMOS synchronization is achieved using a programmable pulse delay generator (Quantum Composers, Emerald 9250) that takes a 20 kHz master signal from the MIR laser and outputs a 40 kHz signal to trigger the CMOS camera. This maximizes the duty cycle of measurements by allowing alternating hot and cold frames to be acquired within a given movie. Subsequent CMOS movie processing entails subtracting cold frames from hot frames to yield final wIR-PHI images. High-speed data acquisition therefore results in an effective photothermal frame rate of 20 kfps, which is a 16-fold increase compared to a previously established widefield photothermal frame rate of 1.25 kfps.[22] wIR-PHI images in **Figures 2-6** have been interpolated. All analyses, however, are conducted on raw images. Further technical details regarding the MIR laser/CMOS camera synchronization, along with a programmatic outline of hot and cold frame subtraction, image processing, and effective wIR-PHI frame rate estimation can be found in the **SI** and in **Figures S1-S3**. IR-PHI data is processed as previously described and involves lock-in amplification of probe signals at the MIR pump laser repetition rate.[23]

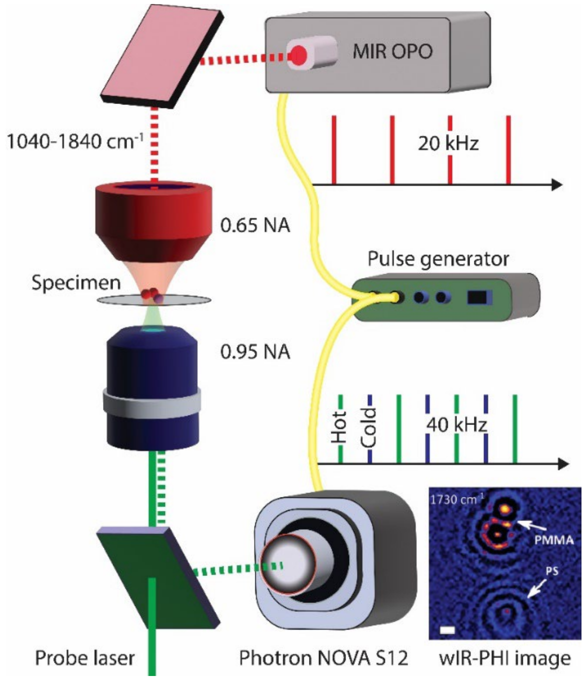

Figure 1. wIR-PHI schematic, consisting of a pulsed, MIR pump laser, a CW, visible wavelength probe laser, a programmable pulse delay generator, a high-speed CMOS camera, and high NA reflective and refractive objectives aligned in a counterpropagating geometry.

Comparing wIR-PHI to IR-PHI

Figure 2 now compares wIR-PHI and IR-PHI images of individual r=130±10 (N=327) nm PMMA and r=210±6 nm (N=100) PS nanoparticles (Phosphorex). Sizes and size distributions have been established using scanning electron microscopy images of respective ensembles (**Figures S4** and **S5**). wIR-PHI and IR-PHI images have been acquired at 1730 cm^{-1} and 1450 cm^{-1} on resonance with PMMA's C=O stretch and PS's CH_2 bend, respectively.[19,29] **Figure 2a**, in particular, shows a 25 μm^2 wIR-PHI image of three PMMA nanoparticles separated by distances below the MIR diffraction limit. **Figure 2b** is a corresponding (identical area) IR-PHI image of the same three particles. These and other like images (**Figure S6**) highlight wIR-PHI's/IR-PHI's high spatial resolution. Associated wIR-PHI and IR-PHI peak signal-to-noise ratios (SNR) in **Figures 2a** and **2b** are 248±22 and 273±19 respectively. SNR calculations are described in detail in the **SI**.

Of note is the 480-fold difference in data acquisition times between **Figures 2a** and **2b**. Whereas the former wIR-PHI image has been acquired in 2 seconds (2.5 kfps or 5000 frames total, 2500 hot, 2500 cold, 300 ns per frame integration, 1.875 second data transfer processing and software overhead), the latter IR-PHI image was acquired over 16 minutes using standard imaging parameters (100 ms lock-in integration, 390 ms total pixel processing time, including software overhead, 2025 total pixels). wIR-PHI's inherent data parallelization is therefore evident.

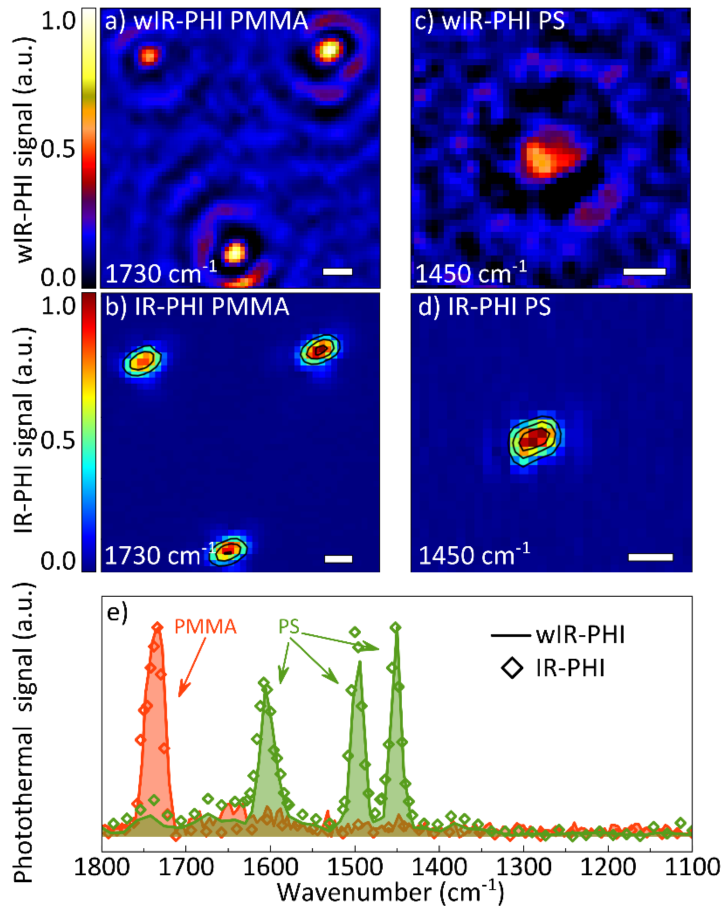

Figure 2. wIR-PHI and IR-PHI images of (a,b) PMMA and (c,d) PS nanoparticles. Scale bars 500 nm. (e) Individual PMMA (orange) and PS (green) nanoparticle wIR-PHI (crosses) and IR-PHI (dashed line) MIR absorption spectra

More dramatic wIR-PHI and IR-PHI data acquisition time differences are possible. To illustrate, in its current implementation, wIR-PHI's field of view is 70 μm^2. Thus, for the same experimental parameters as in **Figure 2**, an image that takes 2 seconds to acquire would require 45 minutes for IR-PHI. This difference becomes even more acute if the CMOS frame number (F) is reduced. For example, reducing F tenfold from 5000 to 500 while maintaining a SNR value above wIR-PHI's current limit-of-detection (LOD, to be discussed shortly) reduces the total image acquisition time to 663 ms (includes data transfer and software overhead). For IR-PHI, reducing the lock-in integration time to 30 ms results yields a 160 ms pixel processing time (includes software overhead). A total IR-PHI data acquisition time is still on the order of 19 minutes.

Other differences between wIR-PHI and IR-PHI images exist. Most notable are Airy diffraction rings in the former and absent in latter. This stems from the scanning nature of IR-PHI where photothermal contrast is measured locally by focusing the visible probe laser. In this modality, diffraction effects only occur when the beam is localized at the particle. By contrast, wIR-PHI's inherent widefield (probe) illumination introduces diffractive effects into acquired images. These diffraction rings can be eliminated using a low coherence light source, as will be demonstrated shortly. **Figures 2c-d** show an identical comparison of wIR-PHI and IR-PHI images for a single PS nanoparticle. Analogous wIR-PHI and IR-PHI images for other PMMA nanoparticle sizes can be found in the **SI** (**Figure S6**).

Figure 2e now shows associated wIR-PHI and IR-PHI absorption spectra for imaged *r*=130 PMMA and *r*=220 PS nanoparticles. For PMMA, both wIR-PHI and IR-PHI show a single 1730 cm^{-1} C=O resonance. For PS, both wIR-PHI and IR-PHI exhibit three resonances. The first two are aromatic ring stretches at 1600 cm^{-1} and 1500 cm^{-1}. A third 1450 cm^{-1} resonance arise from PS's CH_2 bend. Observed single nanoparticle wIR-PHI and IR-PHI resonances for PMMA and PS nanoparticles agree.

wIR-PHI SNR ratio and limit-of-detection

To establish wIR-PHI's SNR dependency with *F* and its LOD, different-sized PMMA nanoparticles have been imaged under the same experimental conditions. For PMMA nanoparticles, four radii are used: *r*=97±12 nm (*N*=100), *r*=130±10 nm (*N*=327), *r*=233±7 nm (*N*=100), and *r*=556±39 nm (*N*=100). In what follows, these PMMA sizes are referred to as 97, 130, 233, and 556 nm nanoparticles. **Figure S4** of the **SI** shows SEM images and sizing histograms used to establish nanoparticle sizes.

Figure 3a now shows acquired peak SNR ratios for wIR-PHI images of different-sized PMMA nanoparticles. As in **Figure 2**, a CMOS frame integration time of 300 ns is used across all images. Varied, however, is *F*, the total number of hot and cold frames acquired, which ranges from *F*=2 to $F=10^4$. As expected, peak SNR-values increase with increasing *F* for all particle sizes. The SNR data generally follow a square root dependence for all sizes wherein power law growth coefficients for SNR $\propto F^{\alpha}$ are α=0.46 (*r*=97 nm), 0.45 (*r*=130 nm), 0.43 (*r*=233 nm), and 0.47 (*r*=556 nm).[30] The bottom of **Figure 3a** highlights wIR-PHI SNR differences by showing associated images of a *r*=130 nm nanoparticle imaged with *F*=50 and *F*=5000.

wIR-PHI's limit-of-detection (LOD) is subsequently established by acquiring data on 20 individual nanoparticles for each size with *F*=5000. Two LOD values are extracted wherein the first is a peak cross section LOD (LOD_{peak}) and the second is an integrated cross section LOD ($LOD_{integrated}$). The former uses SNR-values, obtained by dividing the peak wIR-PHI signal of a nanoparticle with its corresponding background noise standard deviation. The second calculates the integrated wIR-PHI signal of a nanoparticle (summed contrast across a 97×97 nm area) to the same background noise standard deviation.

Figure 3b shows that peak cross section SNR-values decrease from SNR~2600±560 for *r*=556 to SNR~140±90 for *r*=97 nm. Associated integrated cross section SNR-values decrease from 12700±3400 to 500±330 for the same size range (**Figure S7**). Observed linear decreases of either SNR-values with particle size are rationalized by the fact that the photothermal contrast used in these estimates come from fixed particle areas, as defined by the pixel(s) used in the analysis. Expected volumetric dependencies due to absorption cross sections scaling as r^3 therefore reduce to linear scaling. By defining a general LOD for either peak or integrated SNR-values as SNR=5 [22], an effective PMMA nanoparticle wIR-PHI $LOD_{peak,CW}$ is $\sigma_{abs}=1.9\times10^{-16}$ cm^2. This is two orders of magnitude better than a previously established IR-PHI LOD_{peak} of $\sigma_{abs} = 3.0\times10^{-14}$ cm^2.[22] A corresponding $LOD_{integrated,CW}$ is $\sigma_{abs}=1.4\times10^{-18}$ cm^2.

To enhance wIR-PHI image quality, a low coherence, pulsed probe laser (Thorlabs, NPL52C) is incorporated. This laser has a pulse width of 129 ns and a peak pulse power of 145 mW per 70 μm^2 illumination area. The laser is synchronized with the CMOS camera at 40 kHz using the Emerald pulse delay generator. With the pulsed probe laser, corresponding LOD-values are $LOD_{peak,pulsed}=1.7\times10^{-15}$ cm^2 and $LOD_{integrated,pulsed} = 4.3\times10^{-18}$ cm^2 (**Figures 3b** and **S7**). Lower LODs stem from smaller pulsed probe laser intensities. Details about σ_{abs} LOD estimates can be found in the **SI** and in **Figure S8**.

Figures 3b (bottom) and **4** compare wIR-PHI images, acquired using both CW and pulsed probe lasers. **Figure 4**, in particular, compares CW/pulsed wIR-PHI images of identical PMMA nanoparticles for all sizes studied. Evident is that pulsed wIR-PHI images do not contain Airy diffraction rings. This stems from the pulsed laser's low coherence and reveals improvements to wIR-PHI's image quality.

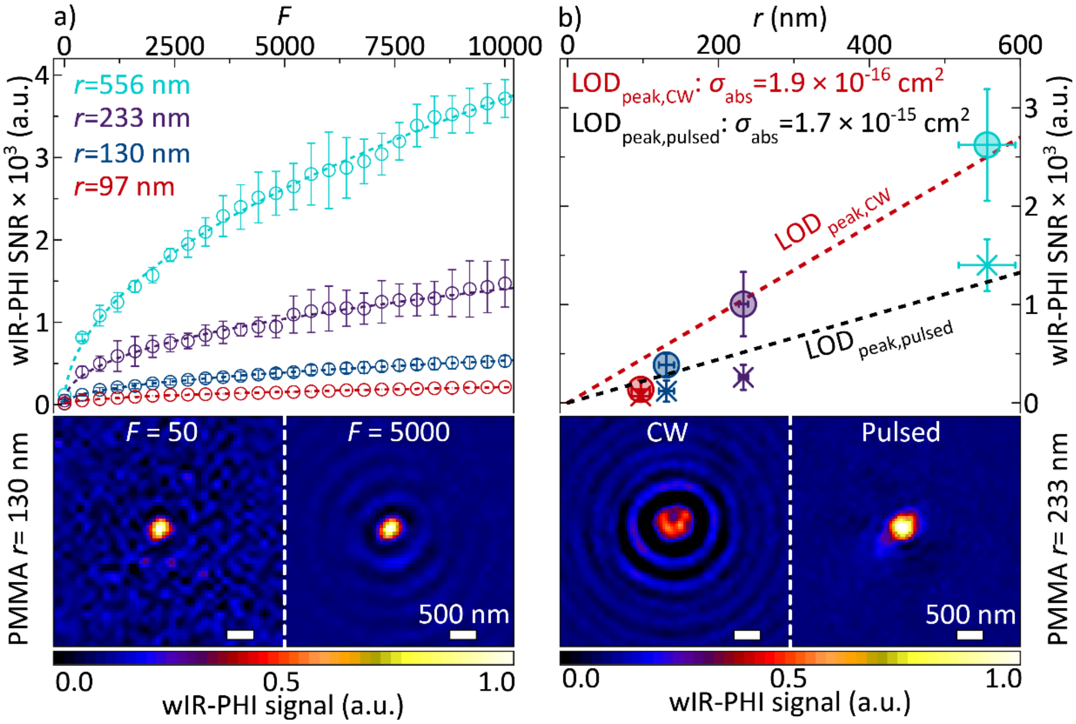

Figure 3. (a) Top: CW wIR-PHI SNR dependence with F for r=97, 130, 233 and 556 nm PMMA nanoparticles. Dashed lines are $SNR \propto F^{\alpha}$ for α=0.46 (r=97 nm), 0.45 (r=130), 0.43 (r=233 nm), and 0.47 (r=556 nm). Bottom: CW wIR-PHI images of r=130 nm PMMA nanoparticles processed using F=50 and F =5000. (b) Top: Peak cross-section SNR dependencies with PMMA nanoparticle size for CW (circles) and pulsed (x) probe lasers. Bottom: wIR-PHI images of r=233 nm PMMA nanoparticles collected using CW or pulsed probe lasers.

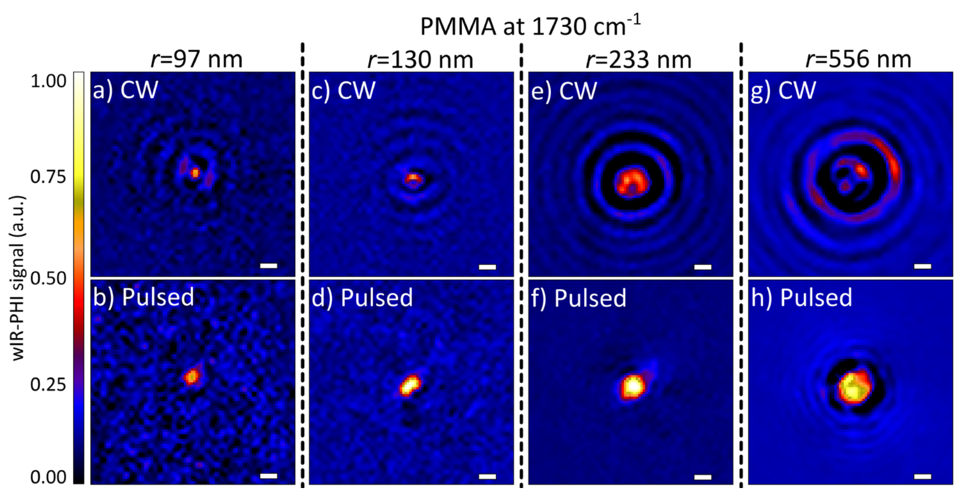

Figure 4. wIR-PHI images of PMMA nanoparticles with varying sizes at 1730 cm^{-1}, acquired using both CW and pulsed probe lasers. All scale bars 500 nm.

wIR-PHI hyperspectral imaging

By synchronizing CMOS data acquisition with MIR pump laser frequency, wIR-PHI hyperspectral imaging is demonstrated on specimens consisting of a mixture of *r*=130 nm PMMA and *r*=514±21 nm (*N*=100, **Figure S5**) PS nanoparticles. In practice, wIR-PHI images are collected sequentially at different MIR energies between 1040-1840 cm^{-1}. Data acquisition involves synchronously tuning the CMOS camera exposure delay relative to MIR laser pulses using home-written Python software.[31]

Figure 5a shows the resulting CW wIR-PHI image stack from where frames acquired at 1730 cm^{-1}, 1600 cm^{-1} and 1450 cm^{-1} are highlighted. At 1730 cm^{-1}, three particles are visible. The top two adjacent particles exhibit strong intensities. The bottom particle is weaker with a three-fold smaller intensity. At 1600 cm^{-1}, the top two particles disappear whereas the bottom particle now exhibits a sizable intensity. At 1450 cm^{-1}, the top two particles remain absent while the bottom particle exhibits an intensity comparable to that seen previously at 1600 cm^{-1}.

wIR-PHI's hyperspectral imaging chemical specificity is therefore apparent. This is made more evident by selecting pixels, associated with identified particles, and plotting their intensities as functions of MIR pump laser wavenumber to construct local MIR absorption spectra. **Figure 5b** shows resulting MIR absorption spectra for the two indicated particles (arrows).

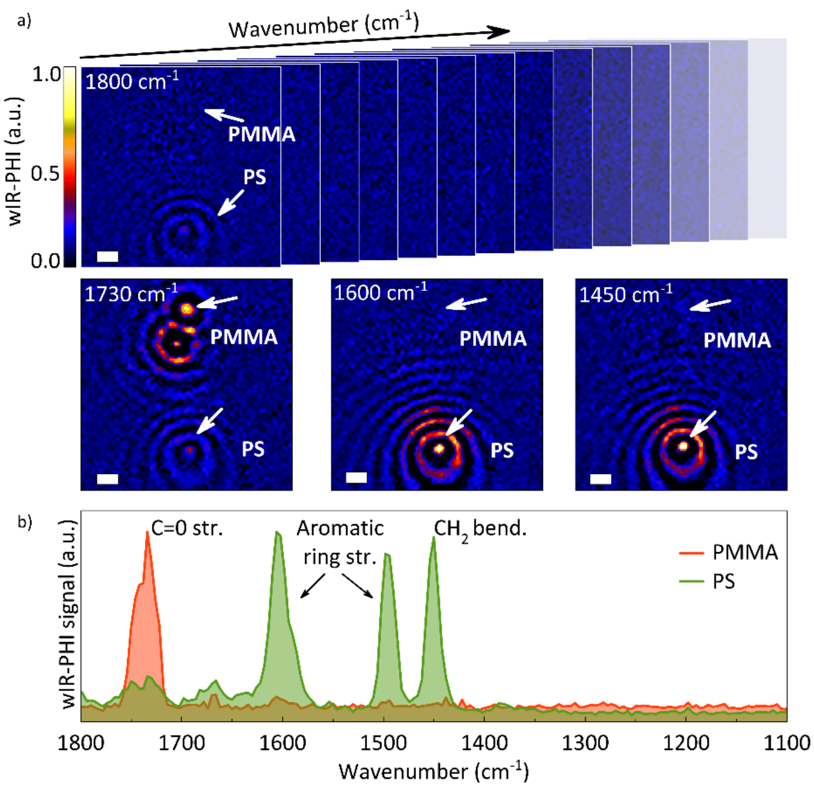

Figure 5. (a) CW wIR-PHI hyperspectral data set with selected images. Scale bars 1 µm. (b) MIR absorption spectra from individual PMMA and PS nanoparticle in the hyperspectral images.

Of note is that the above hyperspectral data, consisting of 4900 spectra and collected across a 70 μm^2 region, has been acquired in 8 minutes. This should be contrasted to the time required by IR-PHI to collect analogous data. To illustrate, at a bare minimum, prior work[22] shows that 2.5 minutes is required per MIR absorption spectra along with approximately 45 minutes per (same area) IR-PHI image. Thus, for two spectra and three images, 140 minutes would be required. Acquiring 200 images to construct an analogous hyperspectral data cube would require ~6 days.

Photothermal dynamics: ns temporal resolution

Because CMOS camera exposure times are short (200-300 ns) and because frame exposures can be electronically delayed on ns-timescales relative to the MIR laser pulse, wIR-PHI can be applied to observe fast photothermal dynamics. Although MIR laser/CMOS camera delays can be generated using an external pulse delay generator, here internal CMOS electronics are used. Delays up to 25 μs are possible with a minimum (temporal) step size of 100 ns. This is comparable to the 50 ns resolution offered by existing step-scan FT-IR techniques[32,33] and is approximately 9 times shorter than the sub-microsecond (915 ns) resolution achieved in alternative widefield MIR imaging techniques.[23] **Figures 2-5** highlight wIR-PHI's super-resolution, which is not possible using step-scan FT-IR.

Figure 6a now shows 2.5 μm^2 (F=5000, 300 ns per frame integration) images of a r=130 nm PMMA nanoparticle acquired at selected delays following the MIR pump pulse. In total, 23 delays between 0-2300 ns have been sampled with data provided as a movie in the SI. The image sequence shows photothermal contrast decaying over ~440 ns. An analogous movie of a r=514 nm PS nanoparticle is also provided.

Figure 6b plots the average photothermal decay (open circles) measured for r=97-556 nm PMMA nanoparticles (three particles each size). In all cases, observed contrast decays exponentially, i.e., wIR-PHI signal $\propto e^{-t/\tau}$ where τ is a material specific decay constant, which can be estimated using the following analytical expression (additional details provided in the SI)[34]

$$\tau = \frac{C}{Ah}. \tag{1}$$

In **Equation 1**, C is a nanoparticle heat capacity (units: J K^{-1}), A is a surface area (units: m^2), and h is a heat transfer coefficient (units: W K^{-1} m^{-2}).[35,36] Fits to experimental decays yield τ-values of τ=210±70 (r=97 nm), 450±100 (r=130 nm), 1100±400 (r=233 nm), and 6200±1100 (r=556 nm) ns.

Dashed lines in **Figure 6b** are predicted decays where h in **Equation 1** has been estimated independently.[35] Resulting theoretical τ-values are τ=200±30 (r=97 nm), 360±60 (r=130 nm), 1160±70 (r=233 nm), and 6610±930 (r=556 nm) ns. The comparison makes evident the good agreement between model and experiment. Details of these τ-value estimates can be found in the **SI**. The data, in whole, thus points to wIR-PHI's ability to simultaneously obtain spatially- and temporally-resolved photothermal data on ns-timescales.

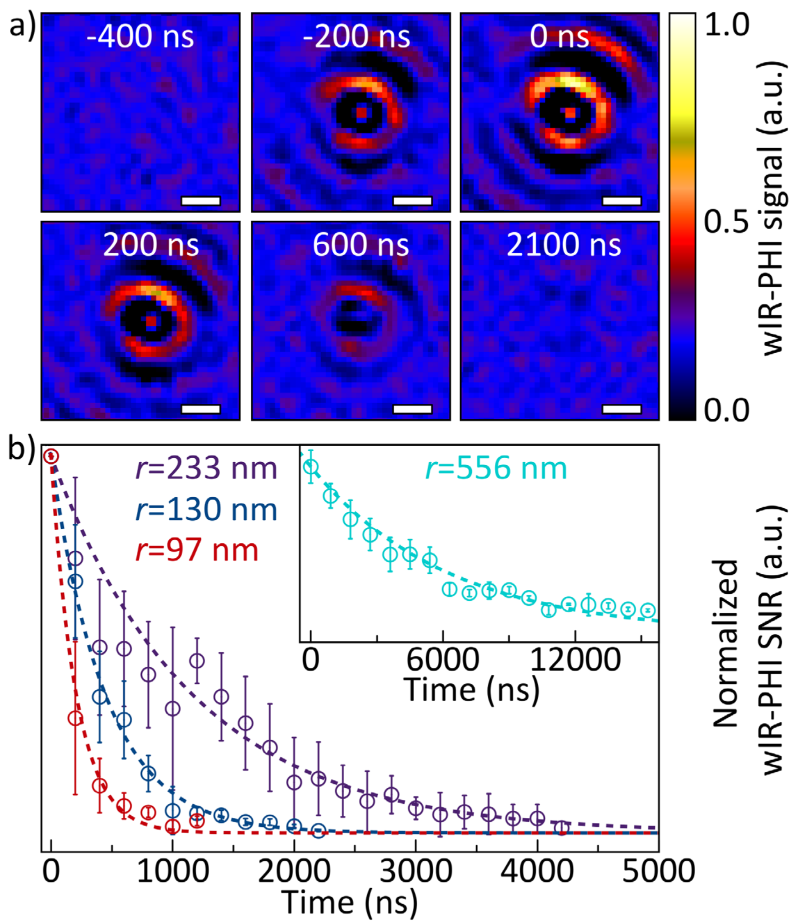

Figure 6. (a) 1730 cm^{-1} CW wIR-PHI images of a r=130 nm PMMA nanoparticle acquired at varying delays, following MIR pulsed excitation. Delay times indicated. All scale bars 500 nm. (b) Corresponding average photothermal contrast decays for r=97, 130, 233, and 556 nm PMMA nanoparticles. Dashed lines are model predictions using independently estimated τ-values.

Conclusion

wIR-PHI represents a new super-resolution, MIR imaging and spectroscopy that enables rapid, large area MIR absorption measurements. Based on a high-speed CMOS camera, wIR-PHI operates in the MIR "fingerprint" spectral region (2.5-10 µm), possesses a ~300 nm spatial resolution, is capable of large area imaging as well as hyperspectral imaging/spectroscopy, and has a temporal resolution on the ns-timescale. wIR-PHI performance is benchmarked by imaging individual PMMA and PS nanoparticles, revealing second timescale images and minute timescale hyperspectral datasets. Temporal resolution on the ns-timescale is also demonstrated. By imaging individual PMMA and PS nanoparticles with radii between r=97-556 nm, a current wIR-PHI peak cross section LOD is $\sigma_{abs}=1.9\times10^{-16}$ cm^2, which is approximately two orders of magnitude better than an analogous IR-PHI peak cross section LOD. This portends well for future uses of wIR-PHI towards MIR imaging and spectroscopic studies of fast chemical, biological, and material processes.

Acknowledgements
M.K. acknowledges the Division of Materials Sciences and Engineering, Office of Basic Energy Sciences. K.K. thanks K. D. Jones for conversations about initial modeling efforts.

Funding
This work was supported by the National Science Foundation (CHE-1954724, and CHE-1902403), U.S. Department of Energy (Award DE-SC0014334), the AFOSR under the MURI:MARBLe project (FA9550-16-1-0362).

Supporting Information Available:
Technical details regarding MIR laser/CMOS camera synchronization, programmatic outline of hot and cold frame subtraction, effective frame rate and image processing, pre- and post-interpolation wIR-PHI images, PMMA and PS nanoparticle SEM images and sizing histograms, wIR-PHI and IR-PHI image comparison, details about LOD estimates, size-dependent peak absorption cross sections for PMMA and PS nanoparticles at 1730 cm^{-1} and 1450 cm^{-1} respectively, movies illustrating the photothermal contrast decay of individual r=130 nm PMMA and r=514 nm PS nanoparticles, and details of τ-value estimates. This material is available free of charge via the internet at http://pubs.acs.

References

(1) Cheng, J. X.; Xie, X. S. Vibrational Spectroscopic Imaging of Living Systems: An Emerging Platform for Biology and Medicine. *Science* **2015**, *350*, aaa8870. DOI: 10.1126/science.aaa8870

(2) Razumtcev, A.; Li, M.; Rong, J.; Teng, C. C.; Pfluegl, C.; Taylor, L. S.; Simpson, G. J. Label-Free Autofluorescence-Detected Mid-Infrared Photothermal Microscopy of Pharmaceutical Materials. *Anal. Chem.* **2022**, *94*, 6512-6520. DOI: 10.1021/acs.analchem.1c05504

(3) Böke, J. S.; Popp, J.; Krafft, C. Optical Photothermal Infrared Spectroscopy with Simultaneously Acquired Raman Spectroscopy for Two-Dimensional Microplastic Identification. *Sci. Rep.* **2022**, *12*, 18785. DOI: 10.1038/s41598-022-23318-2

(4) Kniazev, K.; Pavlovetc, I. M.; Zhang, S.; Kim, J.; Stevenson, R. L.; Doudrick, K.; Kuno, M. Using Infrared Photothermal Heterodyne Imaging to Characterize Micro- and Nanoplastics in

Complex Environmental Matrices. *Environ. Sci. Technol.* **2021**, *55*, 15891-15899. DOI: 10.1021/acs.est.1c05181

(5) Zhang, S.; Kniazev, K.; Pavlovetc, I. M.; Zhang, S.; Stevenson, R. L.; Kuno, M. Deep Image Restoration for Infrared Photothermal Heterodyne Imaging. *Chem. Phys.* **2021**, *155*, 214202. DOI: 10.1063/5.0071944

(6) Pavlovetc, I. M.; Kniazev, K.; Kim, J.; Doudrick, K.; Kuno, M. Photothermal Infrared Imaging: Identification and Visualization of Micro- and Nanoplastics in Environmental Matrices. *Proc. SPIE* **2021**, *11656*, 18. DOI: 10.1021/acs.est.1c05181

(7) Pavlovetc, I. M.; Brennan, M. C.; Draguta, S.; Ruth, A.; Moot, T.; Christians, J. A.; Aleshire, K.; Harvey, S. P.; Toso, S.; Nanayakkara, S. U.; Messinger, J.; Luther, J. M.; Kuno, M. Suppressing Cation Migration in Triple-Cation Lead Halide Perovskites. *ACS Energy Lett.* **2020**, *5*, 2802-2810. DOI: 10.1021/acsenergylett.0c01207

(8) Chatterjee, R.; Pavlovetc, I. M.; Aleshire, K.; Kuno, M. Single Semiconductor Nanostructure Extinction Spectroscopy. *J. Phys. Chem. C* **2018**, *122*, 16443-16463. DOI: 10.1021/acs.jpcc.8b00790

(9) Chatterjee, R.; Pavlovetc, I. M.; Aleshire, K.; Hartland, G. V.; Kuno, M. Subdiffraction Infrared Imaging of Mixed Cation Perovskites: Probing Local Cation Heterogeneities. *ACS Energy Lett.* **2018**, *3*, 469-475. DOI: 10.1021/acsenergylett.7b01306

(10) Pavlovetc, I. M.; Podshivaylov, E. A.; Frantsuzov, P. A.; Hartland, G. V.; Kuno, M. Quantitative Infrared Photothermal Microscopy. *Proc. SPIE* **2020**, *11246*, 13. DOI: 10.1117/12.2545159

(11) Lee, E. S.; Lee, J. Y. Nonlinear Optical Infrared Microscopy with Chemical Specificity. *Appl. Phys. Lett.* **2009**, *94*, 261101. DOI: 10.1063/1.3167286

(12) Li, C.; Zhang, D.; Slipchenko, M. N.; Cheng, J. X. Mid-Infrared Photothermal Imaging of Active Pharmaceutical Ingredients at Submicrometer Spatial Resolution. *Anal. Chem.* **2017**, *89*, 4863-4867. DOI: 10.1021/acs.analchem.6b04638

(13) Zhang, C.; Aldana-Mendoza, J. A. Coherent Raman Scattering Microscopy for Chemical Imaging of Biological Systems. *J. Phys. Photon.* **2021**, *3*, 032002. DOI 10.1088/2515-7647/abfd09

(14) Nasse, M. J.; Walsh, M. J.; Mattson, E. C.; Reininger, R.; Kajdacsy-Balla, A.; Macias, V.; Bhargava, R.; Hirschmugl, C. J. High-Resolution Fourier-Transform Infrared Chemical Imaging with Multiple Synchrotron Beams. *Nat. Methods* **2011**, *8*, 413-416. DOI: 10.1038/nmeth.1585

(15) Editorial. Beyond the Diffraction Limit. *Nat. Photon* **2009**, *3*, 361. DOI: 10.1038/nphoton.2009.100

(16) Löder, M. G. J.; Kuczera, M.; Mintenig, S.; Lorenz, C.; Gerdts, G. Focal Plane Array Detector-Based Micro-Fourier-Transform Infrared Imaging for the Analysis of Microplastics in Environmental Samples. *Environ. Chem.* **2015**, *12*, 563-581. DOI: 10.1071/EN14205

(17) Zhang, D.; Lan, L.; Bai, Y.; Majeed, H.; Kandel, M. E.; Popescu, G.; Cheng, J. X. Depth-Resolved Mid-Infrared Photothermal Imaging of Live Cells and Organisms with Submicrometer Spatial Resolution. *Sci. Adv.* **2016**, *2*, e1600521. DOI: 10.1126/sciadv.1600521

(18) Li, Z.; Aleshire, K.; Kuno, M.; Hartland, G. V. Super-Resolution Far-Field Infrared Imaging by Photothermal Heterodyne Imaging. *J. Phys. Chem. B* **2017**, *121*, 8838-8846. DOI: 10.1021/acs.jpcb.7b06065

(19) Gaiduk, A.; Ruijgrok, P. V.; Yorulmaz, M.; Orrit, M. Detection Limits in Photothermal Microscopy. *Chem. Sci.* **2010**, *1*, 343-350. DOI: 10.1039/C0SC00210K

(20) Aleshire, K.; Pavlovetc, I. M.; Collette, R.; Kong, X. T.; Rack, P. D.; Zhang, S.; Masiello, D. J.; Camden, J. P.; Hartland, G. V.; Kuno, M. Far-Field Midinfrared Superresolution Imaging and Spectroscopy of Single High Aspect Ratio Gold Nanowires. *Proc. Natl. Acad. Sci.* **2020**, *117*, 2288-2293. DOI: 10.1073/pnas.1916433117

(21) Pavlovetc, I. M.; Aleshire, K.; Hartland, G. V.; Kuno, M. Approaches to Mid-Infrared, Super-Resolution Imaging and Spectroscopy. *Phys. Chem. Chem. Phys.* **2020**, *22*, 4313-4325. DOI: 10.1039/C9CP05815J

(22) Pavlovetc, I. M.; Podshivaylov, E. A.; Chatterjee, R.; Hartland, G. V.; Frantsuzov, P. A.; Kuno, M. Infrared Photothermal Heterodyne Imaging: Contrast Mechanism and Detection Limits. *J. Appl. Phys.* **2020**, *127*, 165101. DOI: 10.1063/1.5142277

(23) Bai, Y.; Zhang, D.; Lan, L.; Huang, Y.; Maize, K.; Shakouri, A.; Cheng, J. X. Ultrafast Chemical Imaging by Widefield Photothermal Sensing of Infrared Absorption. *Sci. Adv.* **2019**, *5*, eaav7127. DOI: 10.1126/sciadv.aav7127

(24) Paiva, E. M.; Schmidt, F. M. Ultrafast Widefield Mid-Infrared Photothermal Heterodyne Imaging. *Anal. Chem.* **2022**, *94*, 14242-14250. DOI: 10.1021/acs.analchem.2c02548

(25) Li, S.; Dai, Z.; Li, L.; Padture, N. P.; Guo, P. Time-Resolved Vibrational-Pump Visible-Probe Spectroscopy for Thermal Conductivity Measurement of Metal-Halide Perovskites. *Rev. Sci. Instrum.* **2022**, *93*, 053003. DOI: 10.1063/5.0083763

(26) Zhang, D.; Lan, L.; Bai, Y.; Majeed, H.; Kandel, M. E.; Popescu, G.; Cheng, J. X. Bond-Selective Transient Phase Imaging via Sensing of the Infrared Photothermal Effect. *Light Sci. Appl.* **2019**, *8*, 116. DOI: 10.1038/s41377-019-0224-0

(27) McDonald, M. P.; Vietmeyer, F.; Aleksiuk, D.; Kuno, M. Supercontinuum Spatial Modulation Spectroscopy: Detection and Noise Limitations. *Rev. Sci. Instrum.* **2013**, *84*, 113104. DOI: 10.1063/1.4829656

(28) Bai, Y.; Yin, J.; Cheng, J. X. Bond-Selective Imaging by Optically Sensing the Mid-Infrared Photothermal Effect. *Sci. Adv.* **2023**, *7*, eabg1559. DOI: 10.1126/sciadv.abg1559

(29) Ahmad, S.; Ahmad, S.; Agnihotry, S. A. Synthesis and Characterization of In Situ Prepared Poly (Methyl Methacrylate) Nanocomposites. *Bull. Mater. Sci.* **2007**, *30*, 31-35. DOI: 10.1007/s12034-007-0006-9

(30) Seitz, P. Image Sensing with Maximum Sensitivity Using Industrial CMOS Technology. *Proc. SPIE* **1997**, *3099*, 22-33. DOI: 10.1117/12.281222

(31) Zaitsev, E. PHI_photron_camera. *GitHub* **2023**. Access on April 20 2023, https://github.com/gliese3/PHI_photron_camera.

(32) Johnson, T. J.; Simon, A.; Well, J. M.; Harris, G. W. Applications of Time-Resolved Step-Scan and Rapid-Scan FT-IR Spectroscopy: Dynamics from Ten Seconds to Ten Nanoseconds. *Appl. Spectrosc.* **1993**, *47*, 1376-1381. DOI:10.1366/0003702934067397

(33) Palmer, R. A.; Manning, C. J.; Rzepiela, J. A.; Widder, J. M.; Chao, J. L. Time-Resolved Spectroscopy Using Step-Scan Fourier Transform Interferometry. *Appl. Spectrosc.* **1989**, *43*, 193-195. DOI: 10.1366/0003702894203101

(34) Zhang, S.; Zhukovskyi, M.; Janko, B.; Kuno, M. Progress in Laser Cooling Semiconductor Nanocrystals and Nanostructures. *NPG Asia Mater.* **2019**, *11*, 54. DOI: 10.1038/s41427-019-0156-4

(35) Incropera, F. P.; DeWitt, D. P.; Bergman, T. L.; Lavine, A. S. Fundamentals of Heat and Mass Transfer, 6th Ed. *John Wiley & Sons* **2006**, 585-586.

(36) Schlünder, E. U.; Churchill, S. W. Heat Exchanger Design Handbook, Hemisphere 2.5.7 **1983**, 513-514.

For Table of Content Use Only

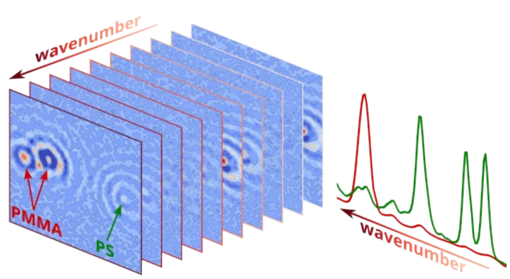

TOC Art

Supplementary information for

Hyperspectral and Nanosecond Temporal Resolution Widefield Infrared Photothermal Heterodyne Imaging

Authors: Kirill Kniazev[a], Evgenii Zaitsev[a], Shubin Zhang[b], Yang Ding[a], Loc Ngo[a], Zhuoming Zhang[a], Gregory V. Hartland[a], Masaru Kuno[a,b]

Affiliations:
[a]Department of Chemistry and Biochemistry, University of Notre Dame, Notre Dame, IN 46556
[b]Department of Physics and Astronomy, University of Notre Dame, Notre Dame, IN 46556

MIR laser/CMOS camera synchronization technical details

The 20 kHz external signal from the M-Squared laser is used as the master trigger for the instrument. A Quantum Composers Emerald pulse delay generator then reads the 20 kHz signal and creates a 40 kHz pulse train that can be delayed relative to the input signal. Possible delays range from 0-24.9 μs. In what follows, delays are generated using the CMOS camera's internal delay electronics (below). This 40 kHz pulse train is then fed into the Photron CMOS camera to enable external synchronization of its frame acquisition. Camera synchronization involves temporally offsetting frame acquisition from MIR laser pulses via the camera's internal electronics (delays from 0-15.5 μs). A home-written Python program was used to control camera image acquisition and subsequent data transfer.

Figure S1 illustrates the synchronization involved in wIR-PHI measurements. MIR laser pulses repeat at 20 kHz. CMOS frame acquisition occurs at 40 kHz. Frames coincident with the MIR laser are referred to as hot frames. Frames between MIR pulses are referred to as cold frames.

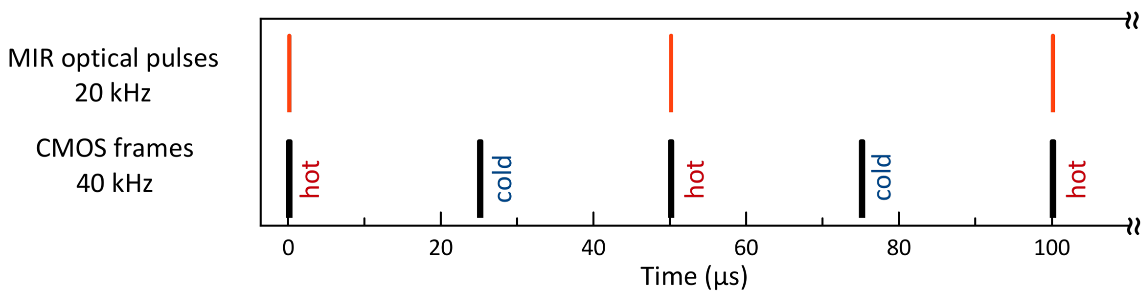

Figure S1. Schematic illustration of MIR laser and CMOS camera synchronization. Hot and cold frames denoted.

wIR-PHI effective frame rate

The effective frame rate of wIR-PHI is determined by the acquisition of "hot" and "cold" frames, which establish the photothermal contrast. In wIR-PHI, the system operates at a frequency of 20 kfps (20,000 fps), acquiring 40,000 "hot" and "cold" frames, with each "hot" frame containing a single MIR laser pulse. **Figure S2** now displays a wIR-PHI image of a single *r*=556 nm PMMA nanoparticle, obtained using a single "hot" and "cold" frame pair.

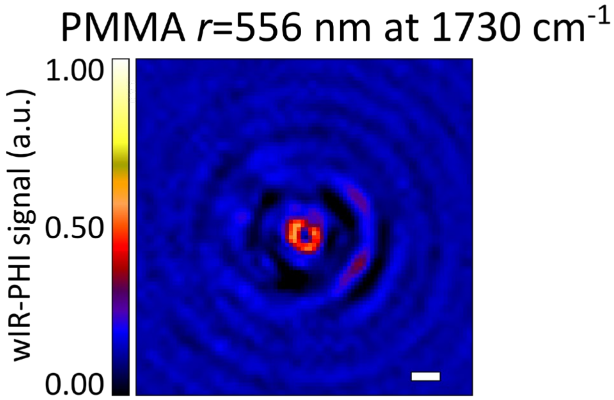

Figure S2. wIR-PHI image of a single *r*=556 nm PMMA nanoparticle processed using only one "hot" and "cold" frame pair.

The effective fps achieved varies depending on the number of frame pairs used to construct wIR-PHI images. For instance, constructing images using one "hot" and "cold" frame pair yields a 20 kfps image rate. Using two sequential "hot" and "cold" frame pairs yields a 10 kfps image rate. 2500 sequential "hot" and "cold" frame pairs yields a 2.5 kfps image rate.

It's important to emphasize that the 1.875 s "data transfer processing and software overhead" does not contribute to the instrument's imaging speed. This time refers only to the speed of the final data transfer and processing. The effective fps, on the other hand, is defined by the number of summed "hot" and "cold" frame pairs, used to construct wIR-PHI images, as stated above.

Image processing

The CMOS camera operates at 40 kHz and collects 256×256 pixel frames. The total frame number, *F*, includes both hot and cold frames. A home-written Python program separates hot and cold frames from a given CMOS movie into two different 3-dimensional (3D) arrays. Intensities in each (x,y) coordinate of a hot/cold 3D array are then summed. What emerges are summed hot and cold images. A wIR-PHI image is obtained by subtracting the summed cold image from the summed hot image. To quadruple the image resolution (from 256×256 to 512×512 pixels) the 'interpolate.interp2d' function from the SciPy Python library is used. [1]

Figures S3 a, **c**, **e**, and **g** show representative raw wIR-PHI images. **Figures S3 b**, **d**, **f**, and **h** show interpolated wIR-PHI images.

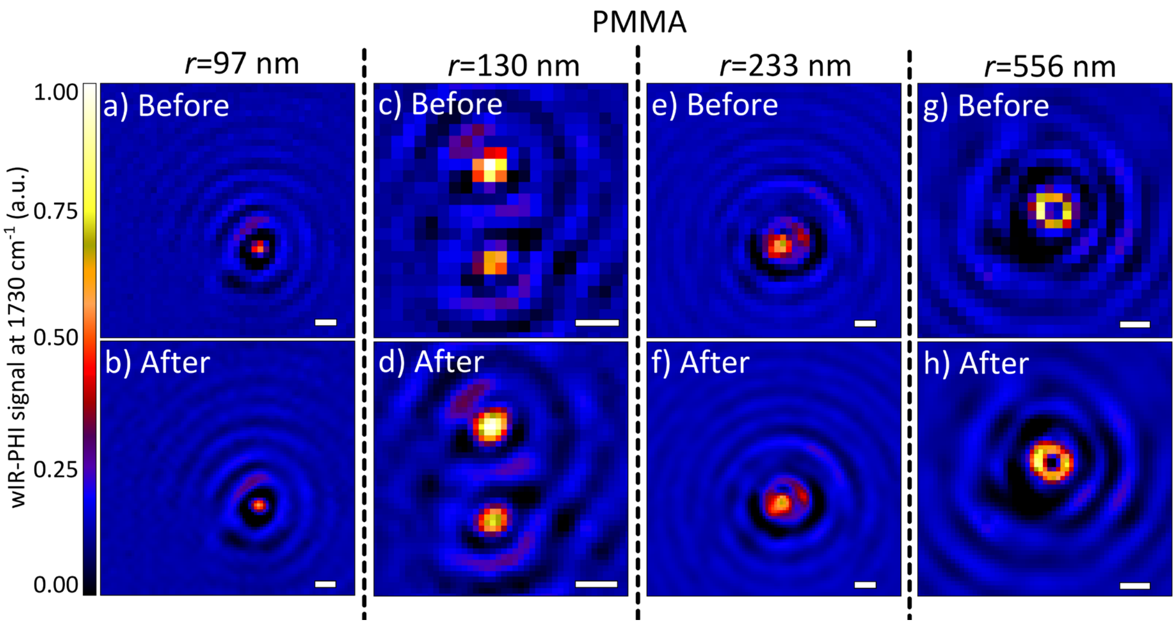

Figure S3. Before (a, c, e, g) and after (b, d, f, h) interpolation wIR-PHI images of different-sized PMMA nanoparticles. All scale bars 500 nm.

wIR-PHI signal-to-noise estimates

Peak SNR estimates use the maximum signal from a particle and divide it with the standard deviation of noise in the illuminated region. 20×20 pixel sections of images that do not contain Airy rings are used for this. Integrated SNR estimates uses the integrated signal from 7×7 pixel sections of the image and divide it by the same noise standard deviation used for peak SNR estimates.

Sample preparation

Solutions of PMMA or PS nanoparticles are drop cast onto calcium fluoride coverslips (CaF_2, 0.5 mm thickness, Crystran) and are allowed to dry under ambient conditions. CaF_2 coverslips were cleaned beforehand using methanol and acetone and were then plasma cleaned (Harrick, Nitrogen). For Scanning Electron Microscopy (SEM), specimens were sputter coated with 3 nm of Ir to prevent charging.

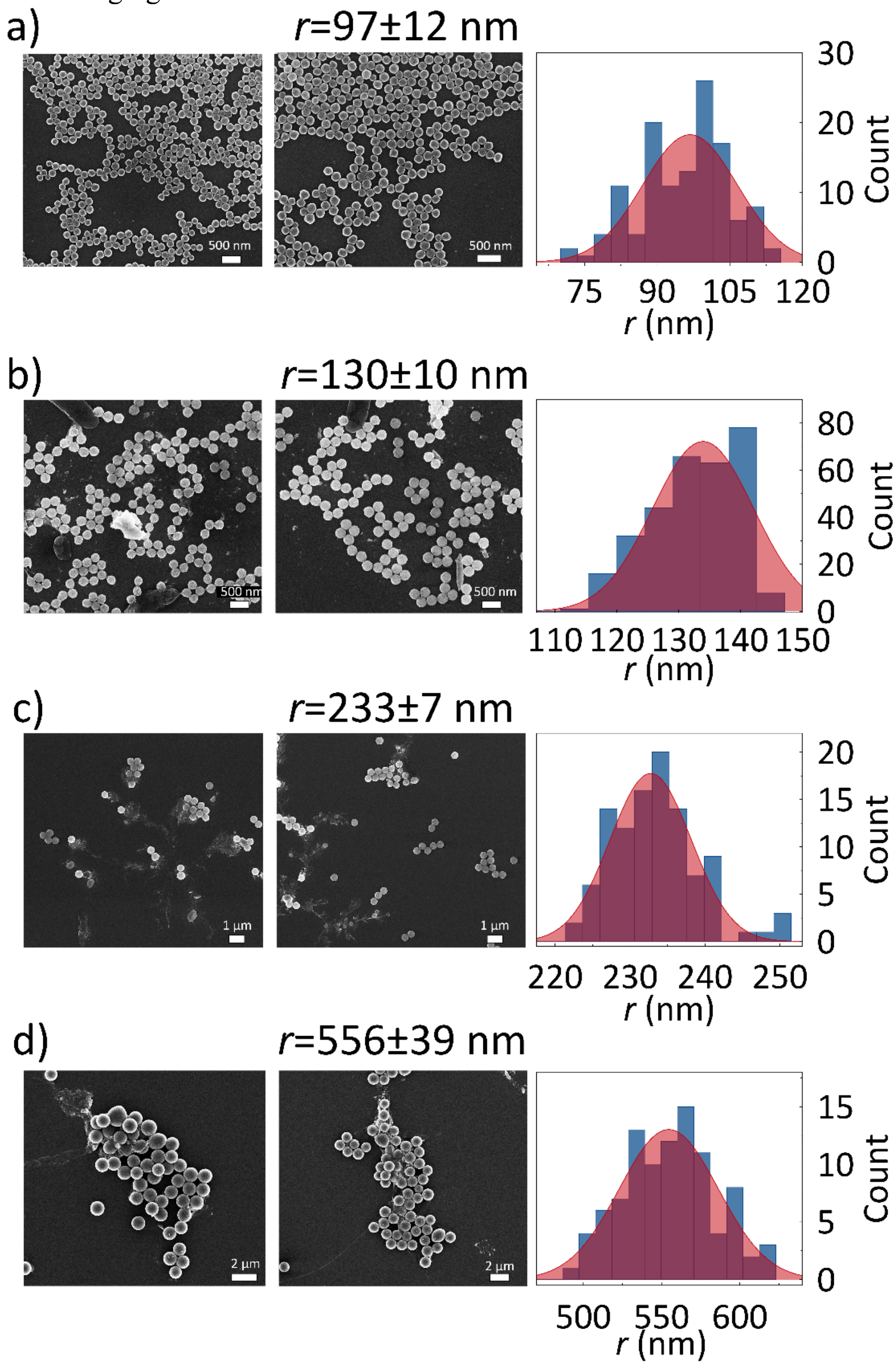

Figure S4. (a-d) SEM images of (a) r=97 nm, (b) r=130 nm, (c) r=233 nm, and (d) r=556 nm PMMA nanoparticles. For all, corresponding size histograms provided.

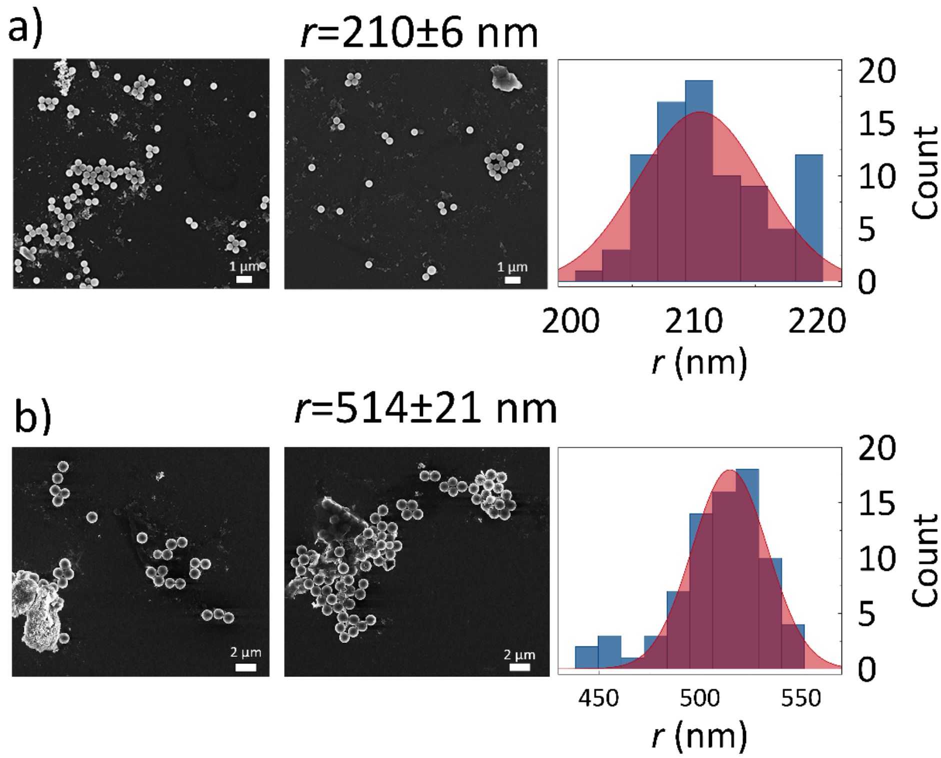

Figure S5. (a, b) SEM images of (a) *r*=210 and (b) *r*=514 nm PS nanoparticles. For all, corresponding size histograms provided.

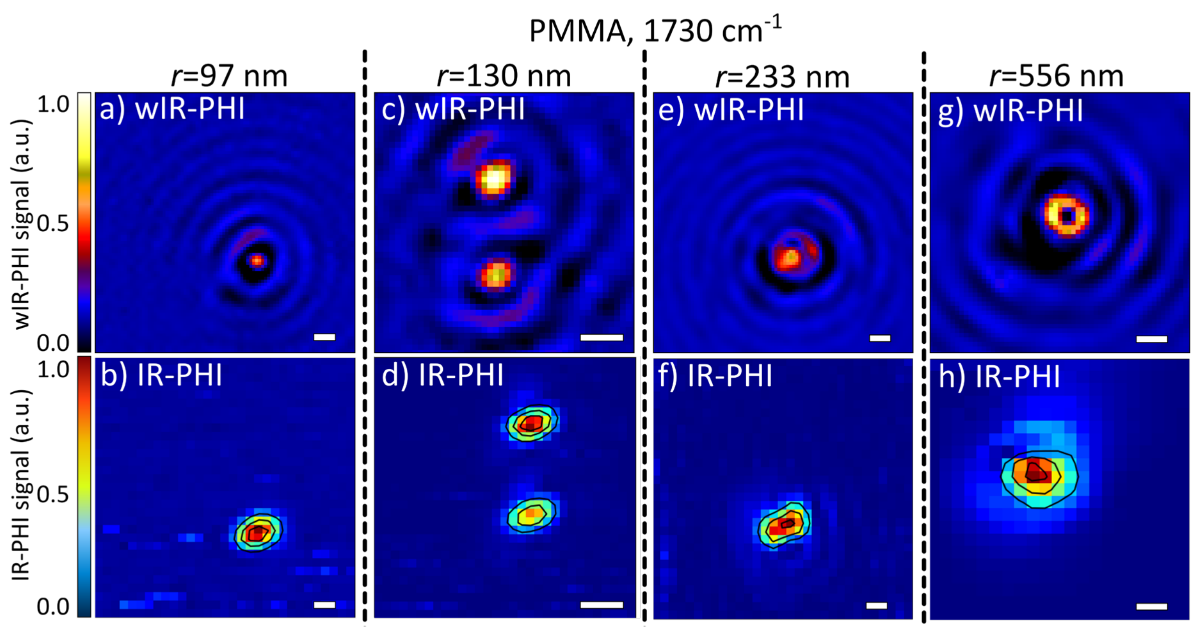

Figure S6. wIR-PHI and IR-PHI images of different-sized PMMA nanoparticles at 1730 cm^{-1}. All scale bars 500 nm.

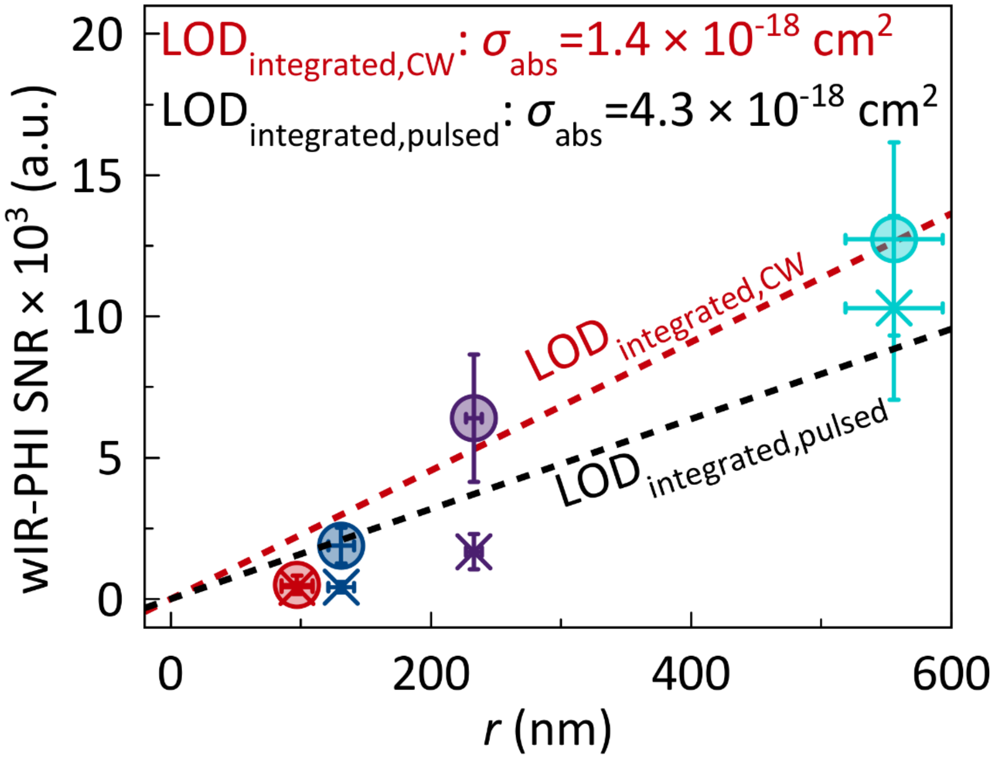

Figure S7. Integrated cross-section SNR dependencies with PMMA nanoparticle size for CW (circles) and pulsed (x) probe lasers.

Absorption cross-section estimates

Absorption cross-sections of PMMA and PS nanoparticles at 1730 cm^{-1} and 1450 cm^{-1}, respectively, were estimated based on published literature data.[2,3] **Equation S1** first extracts an absorption coefficient (α) from experimentally-measured absorbance (Abs) data at a given wavenumber

$$\alpha = \frac{\text{Abs}}{l \times \log_{10}(e)}. \tag{S1}$$

In the equation, l is an experimental thickness for measured PMMA and PS thin films.

Equation S2 calculates a corresponding absorption cross section (σ_{abs})

$$\sigma_{\text{abs}} = \alpha \times V \tag{S2}$$

where V is the volume of the material in the illuminated region.

To estimate the cross section of an individual chromophore, σ_{abs} is divided by the number of absorbers ($N_{\text{absorbers}}$) that are likely present. This latter parameter is found from

$$N_{\text{absorbers}} = \frac{\rho \times V_{\text{NP}}}{m_{\text{monomer}}} \tag{S3}$$

where ρ is the material's density, V_{NP} is the nanoparticle volume ($V_{\text{NP}}=\frac{4}{3}\pi r^3$) and m_{monomer} is the mass of a single PMMA or PS absorber.[4,5]

Figure S8 shows calculated PMMA and PS nanoparticle peak absorption cross-sections for sizes between r=5 and r=750 nm.

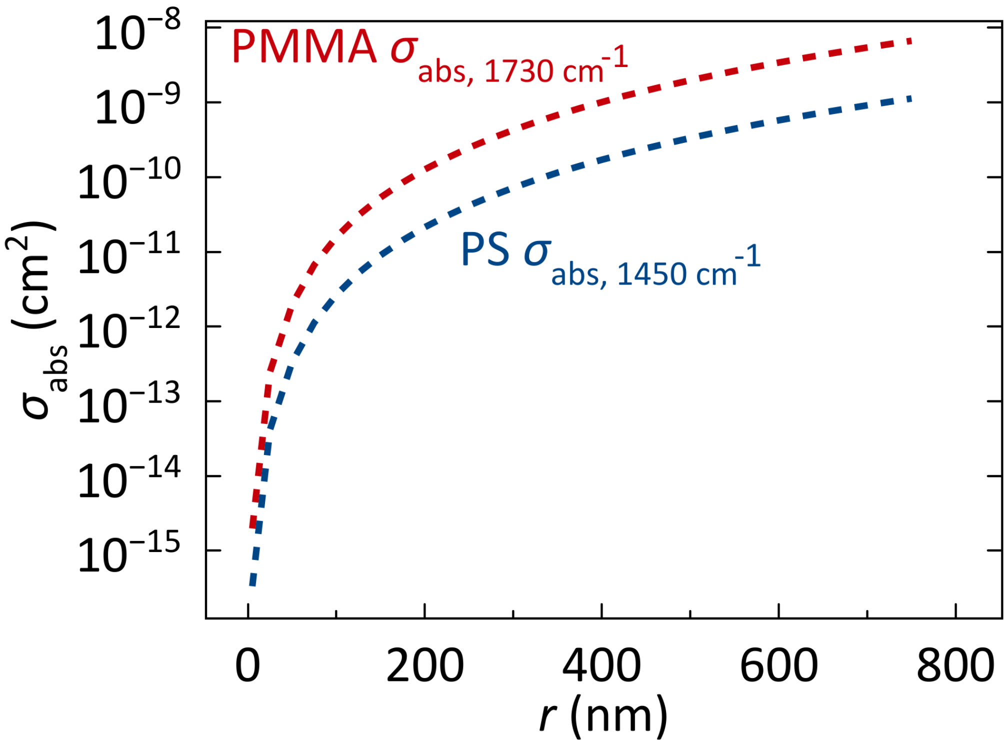

Figure S8. Calculated peak absorption cross-sections for different-sized PMMA and PS nanoparticles at 1730 cm^{-1} and 1450 cm^{-1} respectively.

Nanoparticle thermal decay model

For our polymer particles supported on a solid substrate in air, the majority of the particle surface is in contact with the air, not the support. Because heat loss occurs through the particle surface we simply use a model of a particle in a homogeneous environment:[6]

$$C\frac{\mathrm{d}T}{\mathrm{d}t} = -hA[T(t) - T_0] \quad \text{(S4)}$$

where $C = C_{\mathrm{p,\,NP}} \times m_{\mathrm{NP}}$ is the nanoparticle's heat capacity [units: J K^{-1}; $C_{\mathrm{p,\,NP}}$ is a nanoparticle specific heat capacity which for PMMA is 1368.4 J kg^{-1} K^{-1} [7] and m_{NP} is the nanoparticle mass, $m_{\mathrm{NP}} = \rho \times \left(\frac{4}{3}\pi r^3\right)$ with ρ the polymer density. For PMMA, ρ=1.19 g cm^{-3}], h is a heat transfer coefficient (units: W K^{-1} m^{-2}), A is the nanoparticle geometric surface area (units: m^2), and T_o is ambient temperature. Integration of **Equation S4** yields

$$T(t) = T_0 + (T_{\mathrm{max}} - T_0)e^{-\frac{hA}{C}t} = T_0 + (T_{\mathrm{max}} - T_0)e^{-\frac{t}{\tau}} \quad \text{(S5)}$$

where

$$\tau = \frac{C}{Ah}. \quad \text{(S6)}$$

To independently estimate h for a sphere, an expression from Reference 8 is used

$$h = \frac{\mathrm{Nu}}{(2r)}k, \quad \text{(S7)}$$

where Nu is a Nusselt number and k is the thermal conductivity of air (0.02514 W m^{-1} K^{-1} [9]). For a sphere in a medium

$$\mathrm{Nu} = 2 + \frac{0.589\times \mathrm{Ra}^{1/4}}{[1+(0.469/\mathrm{Pr})^{9/16}]^{4/9}} \quad \text{(S8)}$$

where Ra and Pr are Rayleigh and Prandtl numbers respectively. For small spheres, $\mathrm{Ra} \to 0$. Consequently, $\mathrm{Nu} \cong 2$. Physically, this corresponds to conductive heat transfer into a stationary air medium.[8,10]

SI References

(1) Virtanen, P.; Gommers, R.; Oliphant, T. E.; Haberland, M.; Reddy, T.; Cournapeau, D.; Burovski, E.; Peterson, P.; Weckesser, W.; Bright, J.; Walt, S. J.; Brett, M.; Wilson, J.; Millman, K. J.; Mayorov, N.; Nelson, A. R. J.; Jones, E.; Kern, R.; Larson, E.; Carey, C. J.; Polat, İ.; Feng, Y.; Moore, E. W.; Plas, J. V.; Laxalde, D.; Perktold, J.; Cimrman, R.; Henriksen, I.; Quintero, E. A.; Harris, C. R.; Archibald, A. M.; Ribeiro, A. H.; Pedregosa, F.; Mulbregt, P. SciPy 1.0: Fundamental Algorithms for Scientific Computing in Python. *Nat. Methods* **2020**, *17*, 261-272.

(2) Namouchi, F.; Smaoui, H.; Fourati, N.; Zerrouki, C.; Guermazi, H.; Bonnet, J. J. Investigation on Electrical Properties of Thermally Aged PMMA by Combined Use of FTIR and Impedance Spectroscopies. *J. Alloys Compd.* **2009**, *469*, 197-201.

(3) Vardhan, P. V.; Shukla, L. I. FT-IR Investigations on Effect of High Doses of Gamma Radiation-Induced Damage to Polystyrene and Mechanism of Formation of Radiolysis Products. Radiat. *Environ. Biophys.* **2018**, *57*, 301-307.

(4) NIST Mass Spectrometry Data Center. NIST Chemistry WebBook SRD 69, Methyl Methacrylate. *NIST* **2011**. Access on April 23 2023, https://webbook.nist.gov/cgi/cbook.cgi?ID=C80626&Mask=200.

(5) National Center for Biotechnology Information. PubChem Compound Summary for CID 7501, Styrene. *PubChem* **2021**. Access on April 23 2023, https://pubchem.ncbi.nlm.nih.gov/compound/Styrene.

(6) Winterton, R. H. S. Newton's Law of Cooling. *Eur. J. Phys.* **2002**, *23*, 205-212.

(7) Soldera, A.; Metatla, N.; Beaudoin, A.; Said, S.; Grohens, Y. Heat Capacities of Both PMMA Stereomers: Comparison between Atomistic Simulation and Experimental Data. *Polymer* **2010**, *51*, 2106-2114.

(8) Schlünder, E. U.; Churchill, S. W. Heat Exchanger Design Handbook. Hemisphere 2.5.7 **1983**, 513-514.

(9) Wu, H.; Grabarnik, S.; Emadi, A.; de Graaf, G.; Wolffenbuttel, R. F. Characterization of Thermal Cross-Talk in a MEMS-Based Thermopile Detector Array. *J. Micromech. Microeng.* **2009**, *19*, 074022.

(10) Incropera, F. P.; DeWitt, D. P.; Bergman, T. L.; Lavine, A. S. Fundamentals of Heat and Mass Transfer, 6th Ed. *John Wiley & Sons* **2006**, 585-586.